Journal of Materials Chemistry C

ROYAL SOCIETY OF CHEMISTRY

PAPER

View Article Online
View Journal | View Issue

Cite this: J. Mater. Chem. C, 2025, 13, 17872

Pressure-mediated structural evolution and luminescent properties of $MgGeO_3$:Mn^{2+} nanoparticles: a new candidate for optical high-pressure sensors†

Yihong Liu, Jingyan Liu, Xiaoran Chen, Aditya Kutty, Shanheng Yin, Lijia Liu * and Yang Song *

Received 28th May 2025,
Accepted 17th July 2025

DOI: 10.1039/d5tc02080h

rsc.li/materials-c

A nanosized near-infrared (NIR)-emitting phosphor, Mn^{2+}-doped $MgGeO_3$ (MGO:Mn), was found to exhibit remarkable pressure-dependent color-changing properties over a broad pressure range. The emitting center, Mn^{2+}, when excited with 360 nm UV radiation, emits NIR light at 675 nm under ambient conditions, originating from the $^4T_1 \rightarrow {}^6A_1$ d–d transition. During compression, this emission exhibits a prominent red shift at a rate of 5.43 nm GPa^{-1} until the applied pressure reaches 10.5 GPa. The correlation between the structure and luminescent properties of MGO:Mn under the influence of applied pressure was thoroughly investigated using *in situ* characterization methods, including Raman spectroscopy, X-ray diffraction, and photoluminescence spectroscopy. A partially reversible phase transformation of the $MgGeO_3$ from *Pbca* to *C*2/*c* was observed, which was responsible for the change in the crystal field strength surrounding Mn^{2+}. These findings demonstrate that MGO:Mn is a promising candidate for a non-contact luminescence-based manometer in high pressure applications.

Introduction

High pressure has become a powerful tool for novel material synthesis and discovery. The compression process modifies interatomic distances and the relative atomic positions, producing new structures with unique electrical, magnetic, and optical properties.[1–3] In pressure-mediated materials engineering, precise control and monitoring of the applied high pressure are essential. On a laboratory scale, the high-pressure environment is achieved using a diamond anvil cell (DAC), which generates pressure up to a few hundred GPa.[4] To monitor the pressure inside a DAC, an inorganic phosphor whose luminescence has a direct correlation with the applied pressure is co-loaded with the sample as a pressure gauge.[5] Ruby (Al_2O_3:Cr^{3+}) is one of the most commonly used pressure gauges in a DAC.[6] Under ambient conditions and at room temperature, the main luminescence peak for ruby is located at 694 nm, known as the R1 line, originating from the $^2E \rightarrow {}^4A_2$ transition of the Cr^{3+} 3d electrons.[7] This R1 emission undergoes red shift at a rate of $d\lambda/dP$ = 0.36 nm GPa^{-1} from ambient up to 150 GPa.[8,9] Although ruby has a wide working spectral range, the $d\lambda/dP$ value is relatively small, making it less sensitive to a smaller pressure change. One strategy to increase $d\lambda/dP$ is to choose a host lattice whose structure change is more sensitive to the applied high pressure, by effectively altering the crystal field strength of the Cr^{3+} color center. For example, MgO:Cr^{3+} and $YAlO_3$:Cr^{3+} give off luminescence similar to ruby under ambient conditions, but their luminescence exhibits a larger shift rate of $d\lambda/dP$ = 0.504 nm GPa^{-1} and 0.7 nm GPa^{-1}, respectively.[10,11]

One issue with Cr^{3+}-based phosphors is that the characteristic Cr^{3+} emission consists of several peaks in addition to the most intense R1 line. Under ambient conditions, these peaks can be well-resolved. However, luminescence peaks typically broaden and decrease in intensity as the pressure increases. The peak center of the R1 emission becomes indiscernible from an adjacent R2 line (692.5 nm under ambient conditions), leading to errors in accurately determining pressure. Similar behavior was also reported in lanthanide ion-doped phosphors, which usually contain multiple emission peaks.[12,13] Therefore, ions that give off a single emission band would serve as a more suitable pressure gauge.

Mn^{2+} is another frequently explored 3d metal ion dopant in optical materials. When situated in an octahedral environment, the Mn^{2+}-doped phosphors emit a single peak in the red/near-infrared region, which originates from the Mn^{2+} $^4T_1 \rightarrow {}^6A_1$ d–d transition.[14] Optical pressure sensors based on Mn^{2+}-doped

Department of Chemistry, Western University, 1151 Richmond Street, London, Ontario, N6A 5B7, Canada. E-mail: lijia.liu@uwo.ca, yang.song@uwo.ca

† Electronic supplementary information (ESI) available. See DOI: https://doi.org/10.1039/d5tc02080h

phosphors have been reported, and they generally exhibit a large pressure-dependent wavelength shift, such as Gd(Mg,Zn)B_5O_{10}:Mn^{2+} ($d\lambda/dP$ = 5.54 nm GPa^{-1})[15] and ZnS/CaZnOS:Mn^{2+} ($d\lambda/dP$ = 6.20 nm GPa^{-1}).[16] A noteworthy example is $NaY_9(SiO_4)_6O_2$:Mn^{2+}, a recently reported red-emitting phosphor explored as a high pressure sensor. The emission centre of this material shifts from 617 nm to 663 nm when the pressure increases to 7.16 GPa, with a remarkably high shift rate of $d\lambda/dP$ = 7 nm GPa^{-1}.[17] To date, most of the phosphors that contain Mn^{2+} dopants have been synthesized using a solid-state method which is conducted at high temperatures (typically above 1200 °C), producing micron-sized crystals.[18–20] The optical response of Mn^{2+}-doped nanophosphors under high pressure has been rarely studied. Nanosized phosphors have several advantages over the microcrystals. They can be synthesized from their solution-based precursors, and the processing temperature is lower than the one used in solid-state synthesis. Moreover, they can be used to measure pressure change within the nanosized region.[21]

$MgGeO_3$ (MGO) is considered a geochemical analogue of silicate.[22,23] Under ambient conditions, MGO has an orthorhombic structure with space group *Pbca*.[23] When the pressure increases to 6 GPa at room temperature, the *Pbca* phase begins to transform into a monoclinic *C*2/*c* phase. The *C*2/*c* phase further transforms into a trigonal $R\bar{2}$ phase, but this only occurs at elevated temperatures.[23,24] The crystal structures of the two room-temperature MGO phases, *Pbca* and *C*2/*c*, are shown in Fig. 1. Each structure contains two unique six-coordinated Mg sites with varying degrees of octahedral distortion. When Mn^{2+} is introduced into MGO as a dopant, it occupies the Mg^{2+} site and produces a single band-like emission at around 680 nm.[25,26] The specific emission wavelength depends on the Mn–O bonding environment.[27,28] Mn^{2+}-doped $MgGeO_3$ (MGO:Mn) nanoparticles (NPs) were first synthesized by a sol–gel method in 2020.[26] However, the particles exhibit irregular shapes and a broad size distribution. Recently, we demonstrated that a hydrothermal method can produce MGO:Mn with high phase purity and uniform particle morphology.[29]

In this work, hydrothermally synthesized MGO:Mn NPs are explored for the first time as potential optical pressure sensors. Using *in situ* vibrational spectroscopy in combination with synchrotron X-ray diffraction measurements, structural characterization up to 11.96 GPa is performed to probe the phase transformations during compression and decompression, enabling the correlation between the pressure and the emitted luminescence to be established. Our work demonstrates that the optical properties of MGO:Mn NPs can be effectively tuned by pressure and provides guidance in designing new pressure-sensitive nanostructured phosphors.

Results and discussion

The as-synthesized MGO:Mn NPs were first characterized for their morphology, with the crystal structure and photoluminescent properties under ambient conditions, as shown in Fig. 2. The morphology of MGO:Mn was examined by TEM, shown in Fig. 2(a), the particles exhibited rod-like shapes with varied lengths (190 ± 60 nm). The average width was measured to be 62 ± 10 nm. XRD confirmed that MGO:Mn NPs had a *Pbca* structure (Fig. 2(b)). The diffraction pattern was identical to that of undoped MGO, which was synthesized using the same method (the morphology exhibited the same shape as MGO:Mn, as shown in Fig. S1, ESI†), suggesting that Mn^{2+} substitution did not alter the lattice parameters. All observed diffraction peaks of MGO:Mn are the same as those of undoped MGO, and match well with the reference pattern of the *Pbca* structure.[28,30] The Raman spectra of the MGO:Mn NPs and undoped MGO were collected under ambient conditions and are presented in Fig. 2(c). Seven characteristic modes from MGO were identified and used in the following analysis, including the Ge–O stretching modes (ν_1, ν_2, and ν_3) and the motions of the bridged oxygens within the pyroxene chains (Ge–O–Ge stretching) (ν_4, ν_5, ν_6, ν_7).[23] The detailed peak position in comparison with the reference data is included in Table S1 (ESI†). MGO:Mn exhibited an additional peak at 445 cm^{-1} associated with the coexisting hexagonal GeO_2.[31] This peak is quite weak and broad compared to other vibration modes, indicating that the hexagonal GeO_2 is in an amorphous form, which cannot be detected by XRD.[32] When excited under

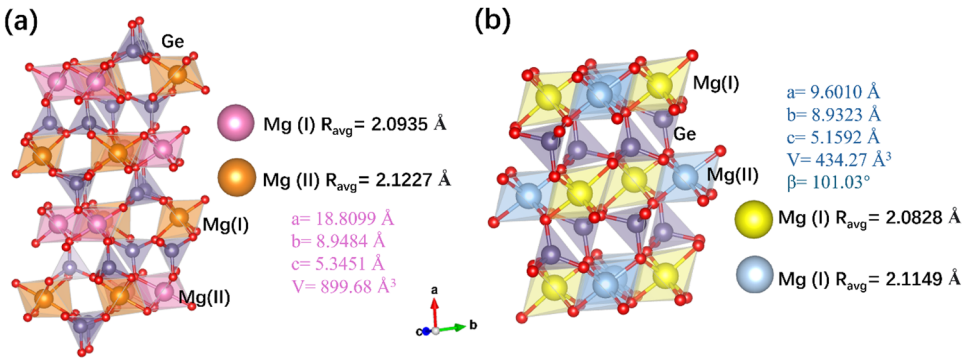

Fig. 1 Crystal structure of (a) *Pbca* and (b) *C*2/*c* $MgGeO_3$. Ge atoms are purple and O atoms are red. Colored octahedra represent Mg in different sites: pink: Mg(I) of *Pbca* $MgGeO_3$, orange: Mg(II) of *Pbca* $MgGeO_3$, yellow: Mg(I) of *C*2/*c* $MgGeO_3$, light blue: Mg(II) of *C*2/*c* $MgGeO_3$,. The calculated average bond length for each Mg^{2+} site in *Pbca* and *C*2/*c* is listed above.

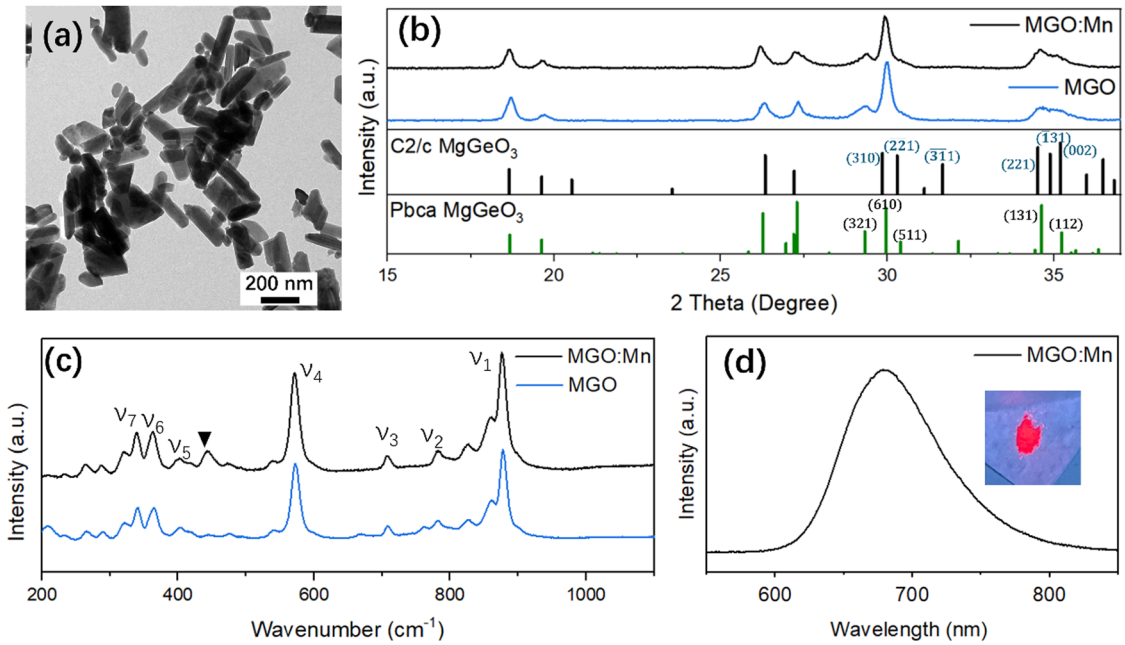

Fig. 2 (a) TEM image of MGO:Mn NPs. (b) XRD pattern of MGO:Mn (at ambient pressure). The standard patterns of $C2/c$[30] and *Pbca* (JCPDF 04-0008-8425) $MgGeO_3$ were also included for comparison. (c) Raman spectra of MGO:Mn and MGO at ambient pressure. The prominent stretching bands from MGO were labelled. The solid triangle marked the stretching mode from GeO_2. (d) PL spectrum and optical photograph (inset) of MGO:Mn were recorded under 254 nm UV light excitation.

a 254 nm UV source, MGO:Mn NPs emit a single, broad emission band centered at 680 nm as shown in Fig. 2(d), which matched well with previous reports.[26,29,33]

To study the pressure-induced phase transformation, *in situ* Raman spectra during compression and decompression were recorded, as shown in Fig. 3(a). It can be clearly seen that the seven vibrational modes from MGO exhibited a blue shift when the pressure increased. This is due to the shortening of the bond length and the resulting bond strengthening. The relative intensities of all the modes remain unchanged until the pressure reaches 4.36 GPa when ν_5 becomes more prominent compared to ν_6 and ν_7. This indicates the onset of a possible phase transformation, as the enhanced intensity of ν_5 matches the feature associated with the high pressure $C2/c$ phase of MGO.[23] On further increasing the pressure, ν_6 and ν_7 quickly diminished, while ν_5 remained and exhibited a consistent shift to a higher frequency. The *Pbca* to $C2/c$ phase transformation was also supported by the change in the ν_1 mode. When MGO is at the *Pbca* phase, ν_1 is accompanied by a shoulder feature at a low wavenumber. This shoulder started to disappear at 4.36 GPa, and when the pressure reached 9.93 GPa, the ν_1 mode only exhibited a single and broad peak, consistent with the feature observed in the $C2/c$ phase.[23]

Fig. 3(b) shows the frequencies of each identified vibrational mode plotted as a function of pressure. From ambient pressure up to 4.36 GPa, the frequency change in all seven modes follows a relatively linear trend, from which the $d\nu/dP$ values can be derived based on a linear regression fit. Beyond 4.36 GPa, the frequencies of ν_1, ν_4, and ν_5 modes exhibit significant deviations from their original pressure dependence. A new linear fit was applied to these three modes, which yielded larger $d\nu/dP$ values, suggesting that the lattice distortion accelerated when the second phase was formed. Meanwhile, the ν_2, ν_3, ν_6 and ν_7 modes became too weak so their pressure dependence cannot be unambiguously monitored beyond 4.36 GPa. The undoped MGO was also in a nanosize and exhibited a rod shape similar to that of MGO:Mn NPs as presented in Fig. S1 (ESI†). The *in situ* Raman spectra for undoped MGO NPs during the compression stage were also measured and presented in Fig. S2 (ESI†). The ν_5 mode becomes stronger when the pressure increases and exceeds the intensity of ν_6 and ν_7 modes at 4.56 GPa, indicating that the undoped MGO has the same phase transition sequence as the MGO:Mn NPs.

The phase transformation behavior of MGO:Mn NPs was also assessed by *in situ* far-infrared (FIR) spectra, shown in Fig. S3 (ESI†). All the IR peaks exhibited a similar blue shift as pressure increased with a clear phase boundary above 5.69 GPa. In particular, the IR band at 499 cm^{-1} under ambient pressure was selected to evaluate the pressure-dependency of the frequency shift. Below 2.15 GPa, the shift rate is calculated to be 3.25 cm^{-1} GPa^{-1} (Fig. S3(b), ESI†). When the pressure exceeded 5.69 GPa, this IR band was completely depleted. Concurrently, a new IR band appeared at 520 cm^{-1} and shifted to a higher frequency of 536 cm^{-1} at 11.43 GPa with a 2.5 cm^{-1} GPa^{-1} shift rate. According to a previous study, at around 520 cm^{-1}, the $C2/c$ phase exhibits a higher band than the *Pbca* phase.[23] Therefore, the phase-dependent IR peaks identified in this study are in good accord with the previous study, indicating that the MGO:Mn is in the $C2/c$ phase at 11.43 GPa. The IR spectrum of the recovered sample upon decompression was

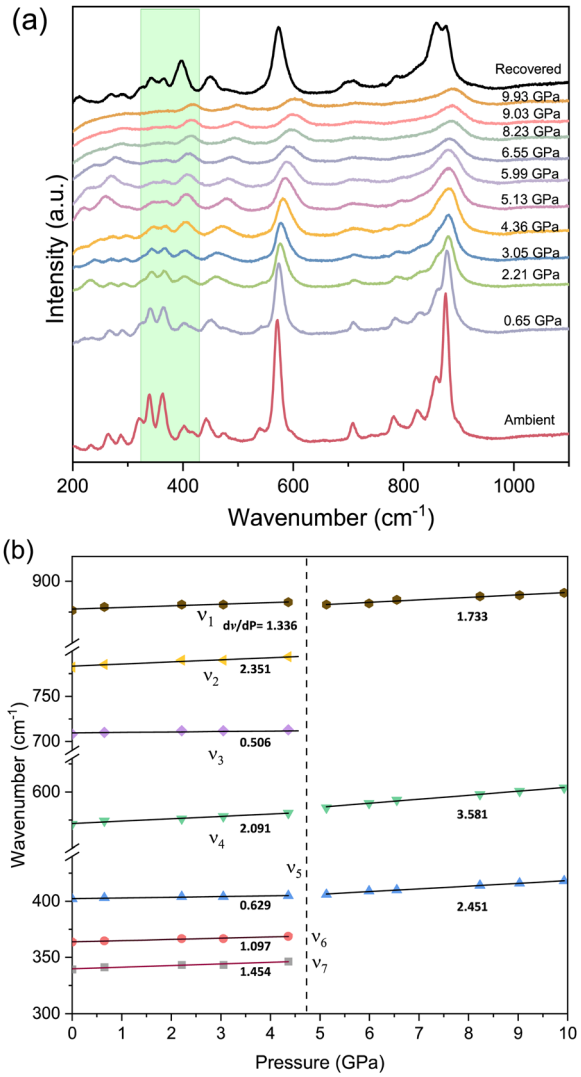

Fig. 3 (a) *In situ* high-pressure Raman spectra of MGO:Mn NPs measured at various pressure points during compression and after decompression. The shaded green area highlights the intensity change of ν_5 against ν_6 and ν_7 modes. (b) Pressure-dependence plot of selected Raman vibrational modes of MGO:Mn NPs for the compression data, with linear regression fits applied for each selected mode to determine the frequency shift rate.

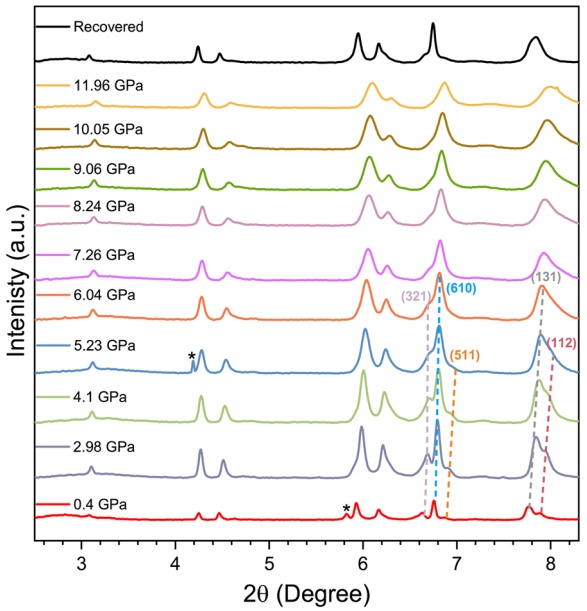

Fig. 4 Pressure-dependent XRD of MGO:Mn NPs. Sharp peaks at around 4.2° and 5.8° (marked as *) are from the Au co-loaded in the DAC cell for pressure calibration purposes.

also collected and plotted in Fig. S3(a) (ESI†), showing that the phase transformation is not fully reversible, consistent with our Raman results.

Since both Raman and far IR measurements suggested that MGO:Mn NPs transformed from the *Pbca* to *C*2/*c* phase upon compression, to obtain a quantitative understanding of the crystal structures under applied pressure, *in situ* synchrotron XRD measurements were performed. The diffraction patterns at various pressures were analyzed using Rietveld refinement. As shown in Fig. 4 during the compression, the *Pbca*-related reflections shift to higher diffraction angles and become broader. This phenomenon is commonly observed in inorganic crystals due to deviatoric stress.[34–36] In addition, peaks of weaker intensities that were well-resolved under ambient pressure began to merge at elevated pressures. For example, the (321) and (511) peaks merged with the (610) peak, and the (112) peak merged with the (131) peak when the pressure increased to 6.04 GPa. Further increasing the pressure (to 7.26 GPa and above) resulted in noticeable changes in the overall diffraction profile, such as the complete disappearance of the (321) reflection, and the asymmetric peak from (131) and (121) combined turned symmetric. These changes are indicative of a phase transformation.

Fig. 5(a)–(c) show the Rietveld refinement results performed on the XRD patterns at two representative high-pressure states (7.26 GPa and 11.96 GPa) and after pressure was released. The refined lattice parameters are summarized in Table 1. It is evident that MGO:Mn NPs exhibit a mixed phase of *Pbca* (45%) and *C*2/*c* (55%) at 7.26 GPa. A complete phase transformation to the *C*2/*c* phase is observed at 11.96 GPa, which agrees with the Raman and far-IR results. After decompression, the *Pbca* phase recovers only to 64%, suggesting that the phase transformation is only partially reversible. The evolution of unit cell parameters (*a*, *b*, *c*, *V*) as a function of pressure was derived from the Rietveld refinement analysis on XRD patterns at each measured pressure. The unit cell parameters normalized to the *Pbca* and *C*2/*c* phases at ambient conditions, respectively, are plotted against the applied pressure, as shown in Fig. 5(d). For the *Pbca* phase, the change in the unit cell parameter *b* is the most significant, indicating a strong anisotropic compression on the MGO:Mn lattice with more compressible MgO_6 octahedra along the *b*-axis than the GeO tetrahedra along the *a*-axis (see Fig. 1(a)). In contrast, for the *C*2/*c* phase that appears at ~5 GPa, all three unit cell parameters exhibit a steady decrease with increasing pressure at a similar compression rate, consistent with the more isotropic packing patterns of the MgO octahedra and GeO tetrahedra for this phase (see Fig. 1(b)).

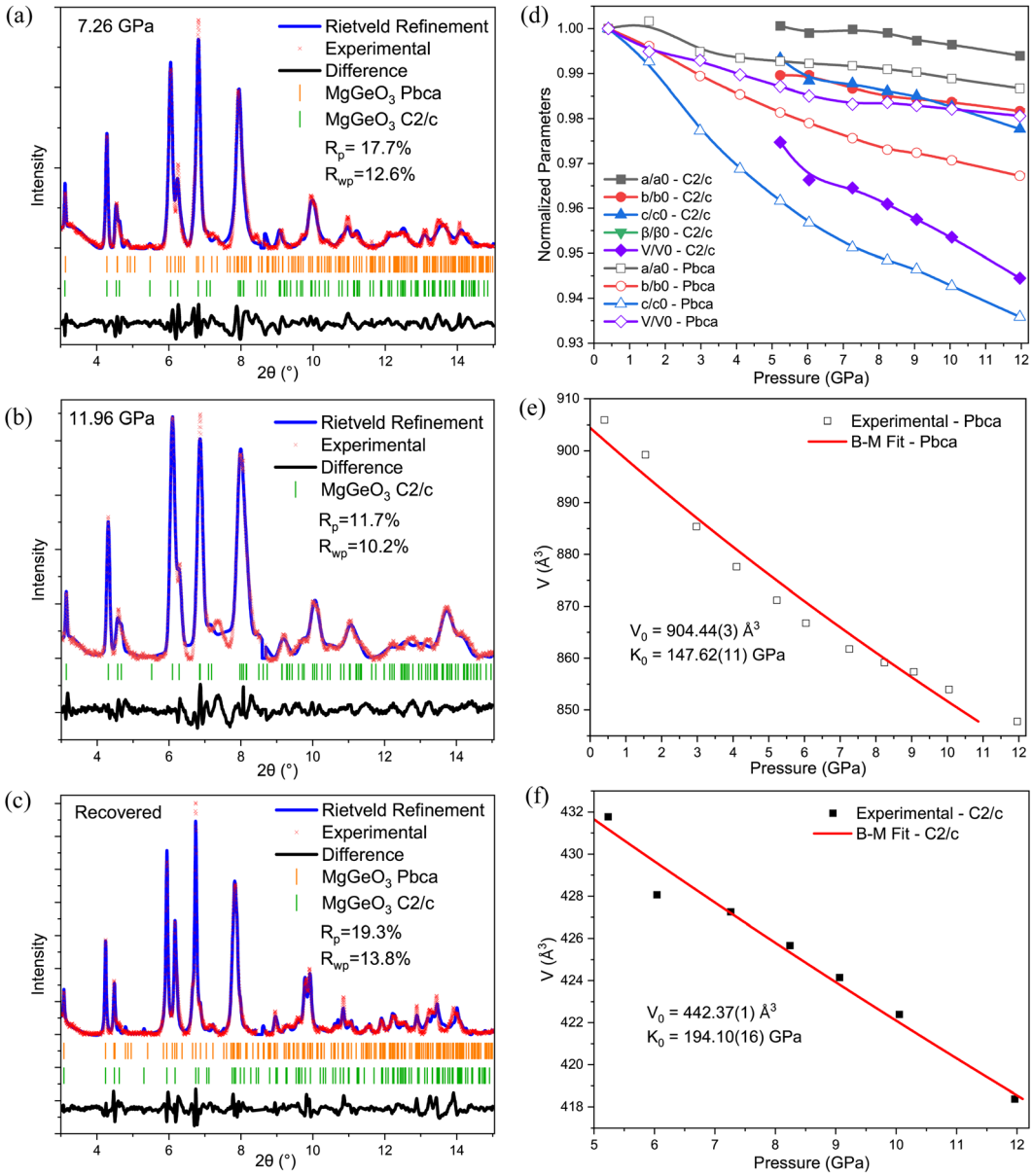

Fig. 5 (a)–(c) Rietveld refinement of the XRD pattern of MGO:Mn compressed under a pressure of 7.26 GPa and 11.96 GPa, and decompressed to the ambient pressure. (d) Normalized cell volume and cell parameters as a function of pressure for MGO:Mn based on the refinement results for the *Pbca* phase (open symbols) and *C*2/*c* phase (closed symbols). (e) Fitting of the second order Birch–Murnaghan EOS for the *Pbca* phase at 0.4-11.96 GPa. (f) Fitting of the second order Birch–Murnaghan EOS for the *C*2/*c* phase at 5.23–11.96 GPa.

Table 1 Phase composition and lattice parameters derived from Rietveld refinement of MGO:Mn NPs at selected pressure points

Pressure	Phase	Phase fraction (%)	Lattice parameters				
			a (Å)	*b* (Å)	*c* (Å)	*β* (°)	*V* (Å^3)
7.26 GPa	*Pbca*	45	18.7112	8.7566	5.2595	90	861.75
	*C*2/*c*	55	9.6579	8.8171	5.1797	104.38	441.08
11.9 GPa	*C*2/*c*	100	9.6008	8.7722	5.1269	104.31	431.79
Pressure release	*Pbca*	64	18.8676	8.9754	5.3494	90	905.89
	*C*2/*c*	46	9.6592	8.9361	5.2439	101.86	452.63

It is noteworthy that compared to a previous study on bulk, undoped MGO, a complete *Pbca* to *C*2/*c* phase transformation was observed at 6 GPa.[23] In our case, the MGO:Mn NPs remain in a mixed phase across a wide pressure range. To reconcile this, we comparatively examined the compression behavior of doped and undoped MGO NPs. As shown in Fig. 3(a) and Fig. S2 (ESI†), the doped- and undoped-MGO NPs exhibit the same phase transition pressure, indicating that the phase stability is enhanced by the small crystal size rather than the dopants, consistent with the observation in the high-pressure studies of other nanostructured materials.[37–41] The compressibility of MGO:Mn was further investigated by fitting both phases with the second order Birch–Murnaghan equation of state (EOS), as shown in Fig. 5(e) and (f). The bulk modulus (K_0) and the volume at 0 GPa (V_0) for the *Pbca* phase were calculated as

147.6(1) GPa and 904.4(3) Å^3(Fig. 6e). The *C*2/*c* phase that appeared after the phase transition at 5.23 GPa shows K_0 = 194.1(2) GPa and V_0 = 442.4(1) Å^3. The bulk modulus of the *C*2/*c* phase at pressures above 5.23 GPa is significantly higher than that of the *Pbca* phase, indicating the lower compressibility of MGO:Mn in the high pressure region, consistent with the trend of other known phases of bulk MGO at even higher pressures.[42]

As demonstrated by the previous studies, the emission wavelength of Mn^{2+} in a ternary Mg–Ge–O compound is highly dependent on the local environment around the Mn^{2+}.[27,28] Therefore, a gradual phase transformation of $MgGeO_3$ from *Pbca* to *C*2/*c* could provide a tunable local environment for Mn^{2+}. In the following, we examine how the pressure-induced phase transformation from *Pbca* to *C*2/*c* influences the luminescence of MGO:Mn NPs. The PL spectra of MGO:Mn NPs were recorded from ambient pressure up to 10.52 GPa under a 360 nm laser excitation. As shown in Fig. 6, with increasing pressure, the PL intensity decreases, and the centre of the emission peak shifts to the longer wavelength. Throughout the applied pressure range, the PL exhibits a total of 75 nm red shift. When the peak centroid position is plotted as a function of pressure, the extent of peak shift can be divided into three regions, represented by a unique dλ/dP value (Fig. 6(c)). Below 1 GPa, dλ/dP = 4.09 nm GPa^{-1}. A more drastic change with dλ/dP = 11.69 nm GPa^{-1} occurs between 1 GPa and 4.08 GPa, and from 4.08 GPa to 10.52 GPa, dλ/dP drops to 5.43 nm GPa^{-1}, which is still more than 10 times larger than that of ruby.

The different slopes indicate that the luminescence from MGO of the *Pbca* phase is overall more sensitive to the pressure change compared to the *C*2/*c* phase. Based on the result from the pressure-dependent XRD measurements (Fig. 5(d)), the unit cell parameters decrease more significantly in the *Pbca* phase compared to the *C*2/*c* phase, which supports the observed optical properties. In either phase, Mn^{2+} retains its octahedral coordination, and the phase transformation from *Pbca* to *C*2/*c* only alters the peak center by modulating the Mn–O distance and degree of distortion. The crystal field strength (D_q) can be determined using the following equation,

$$D_q = \frac{ze^2r^4}{6R^5}$$

where z is the valence of the anion, e is the charge of an electron, r is the radius of the d-wave function, and R is the interatomic distance. Upon compression, the interatomic distance between Mg–O is shortened. When Mn^{2+} substitutes Mg^{2+} in MGO, given that the value of D_q is inversely proportional to the Mn–O distance, a smaller R leads to a stronger crystal field strength and thus a longer emission wavelength. According to the crystal structure in Fig. 1, the average Mg–O bond length of the *C*2/*c* phase is shorter than that of the *Pbca* phase. As a result, the PL redshift continues with the phase transformation, but the dλ/dP is smaller since the *C*2/*c* lattice is more resistant to the applied pressure.

The PL spectra of MGO:Mn upon decompression were measured and are shown in Fig. S4 (ESI†) and Fig. 6(c). The luminescence intensity of MGO:Mn gradually increases as the pressure is released. However, the recovered emission centre

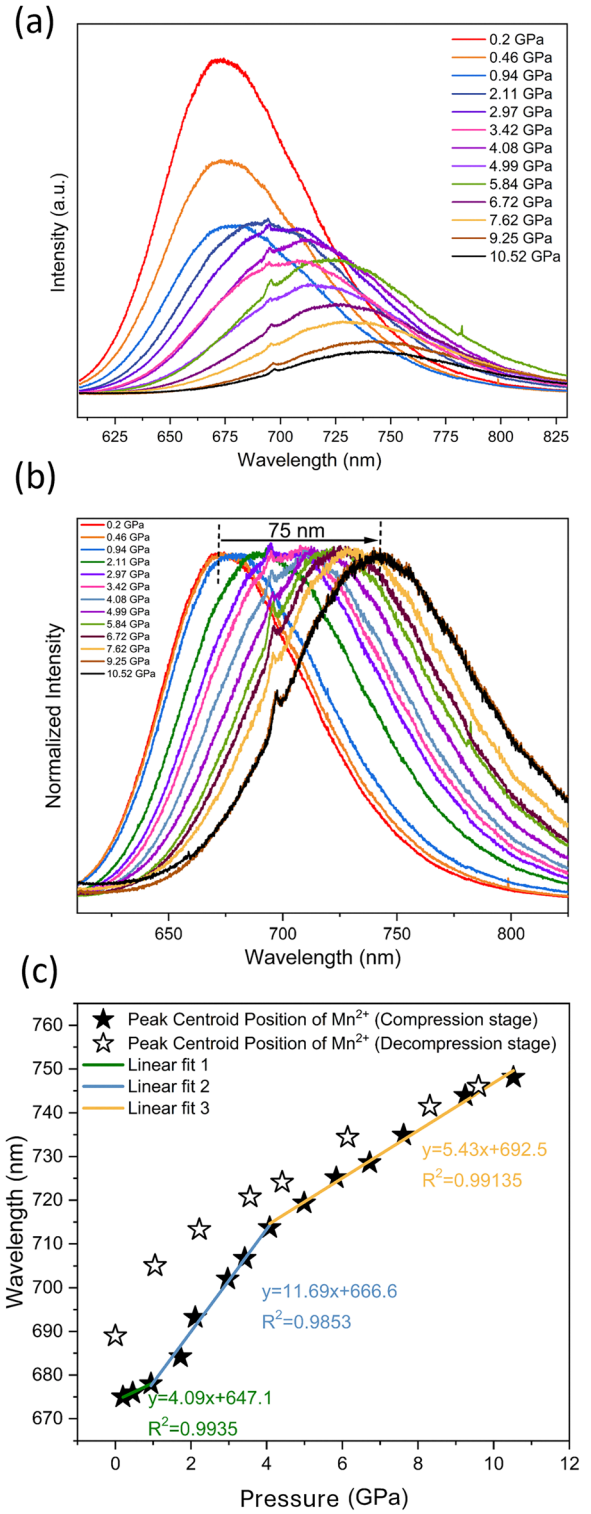

Fig. 6 *In situ* high-pressure compression PL spectra. (a) The emission spectra of MGO:Mn NPs excited at 360 nm. (b) Normalized emission spectra of MGO:Mn NPs excited at 360 nm. The sharp peaks here are from the ruby. (c) Linear regression fitting of emission positions during the compression stage. The emission centre of the decompression stage is included for comparison.

Table 2 Selected examples of red-emitting optical pressure sensors in comparison with MGO:Mn^{2+} in this work

Material	Synthesis method	Crystal size	Sensitivity (nm GPa^{-1})	Pressure sensing limit (GPa)	Centroid range (nm)	Ref.
$CsPb_xMn_{1-x}Cl_3$	Hot injection	Nano-sized 15.5 nm	26.6	0.17–1.23	600–650	46
$Ca_9NaZn_{1-y}Mg_y(PO_4)_7$:$Eu^{2+}$	Solid-state	Micron-sized	5.21	0–16.48	562–634	49
Gd_2ZnTiO_6:Mn^{4+}	Solid-state	Micron-sized	1.11	0–8	706–714	50
AlN:Sm^{2+} (AIN: aluminum nitride)	Direct nitridation	100–200 nm in diameter and 1–2 μm in length	0.133	0–22	686–689	51
$Li_4SrCa(SiO_4)_2$:Eu^{2+}	Solid-state	N/A	5.19	0–10	585–637	52
$Ca_7Mg_2Ga_{6-y}Al_yO_{18}$:$Mn^{4+}$	Solid-state	N/A	1.16	0.5–20.2	721–736	53
$La_3Mg_2SbO_9$:Mn^{4+}	Solid-state	2 μm	1.20	0–11	690–706	54
$MgGeO_3$:Mn^{2+}	Hydrothermal	62 nm in diameter and 190 nm in length	5.43	0–10.5	670–750	This work

does not return to its original position, and the emission intensity remains weaker than the initial value. This is consistent with the phase transformation that is partially reversible, so that the Mn^{2+} ions can occupy the sites associated with both *Pbca* and *C*2/*c* structures. Additionally, structural defects could be created under high pressure which can act as luminescence quenching centres.[43–45]

Table 2 summarizes the red phosphors recently reported for pressure sensing applications, in comparison with MGO:Mn in this work. This comparative table highlights that our MGO:Mn exhibits excellent pressure sensitivity, which is much higher than nearly all the listed phosphors. Unlike most of the pressure sensors in Table 2, MGO:Mn is synthesized at a relatively low temperature and in a nanosized form, offering several advantages over micro-sized phosphors. To be more specific, the use of a hydrothermal method avoids the need for extremely high temperatures typically required in the solid-state method. Moreover, the nanosized MGO:Mn can be used to examine pressure in extremely small regions. Although the pressure sensitivity for MGO:Mn is lower than that of a nano-sized Mn^{2+}-doped cesium lead chloride perovskite with a high sensitivity of $d\lambda/dP$ = 26.6 nm GPa^{-1},[46] our MGO:Mn offers a much broader working range. A similar situation applies to a recently reported double perovskite $Cs_2Ag_{0.6}Na_{0.4}InCl_6$, which shows extremely high sensitivity ($d\lambda/dP$ = 112 nm GPa^{-1}) but only works in a low pressure range from ambient to 4 GPa.[47] Some other pressure sensors, such as $Sr_2MgSi_2O_7$:Eu^{2+}/Dy^{3+},[48] can operate in kinetic mode but still require solid-state synthesis, which limits their accessibility. All together, our MGO:Mn combines a high pressure sensitivity, a broad working range, and a nanosized scale. These advantages make MGO:Mn one of the most promising pressure sensors among the current reported manometers.

Conclusions

In summary, this study investigates the effect of pressure on the structural and luminescence properties of MGO:Mn NPs at room temperature, utilizing *in situ* Raman spectroscopy, synchrotron far-IR spectroscopy, X-ray microdiffraction and photoluminescence spectroscopy. XRD refinement revealed that increasing pressure induced a phase transformation from *Pbca* to *C*2/*c*, which commenced at approximately 5 GPa and is fully completed by 11 GPa. However, upon decompression, the phase transformation was found to be only partially reversible; the refinement indicated that only 64% of the *C*2/*c* phase reverted to the *Pbca* phase. The phase transition also influences the emission properties of the NPs. The PL emission of MGO:Mn, centered at 675 nm with an excitation wavelength of 360 nm, exhibited a red shift, ultimately shifting to 750 nm at 10.58 GPa, demonstrating high-pressure sensitivity ($d\lambda/dP$ = 5.43 nm GPa^{-1}). Notably, the emission intensity remained high at 10.58 GPa. These findings suggest that MGO:Mn NPs are a promising candidate for optical pressure-sensing applications.

Experimental section

Materials

Magnesium nitrate hexahydrate ($Mg(NO_3)_2{\cdot}6H_2O$, ACS reagent > 99%), germanium oxide (GeO_2, hexagonal phase, ≥ 99.99% trace metal basis) and ammonium hydroxide (NH_4OH, 35 wt%), were purchased from Sigma-Aldrich. Manganese(II) chloride tetrahydrate ($MnCl_2{\cdot}4H_2O$, ≥99.99% metal basis) was purchased from Alfa-Aesar. Sodium hydroxide (NaOH, pellets) was purchased from Caledon. Type-I water with a resistivity of 18.2 MΩ-cm purchased from Thermo Scientific was used as a solvent in the experiment. All chemicals were used as received.

Sample preparation

The MGO:Mn NPs were synthesized using a hydrothermal method.[29] Briefly, 0.654 g GeO_2 was first dissolved in 14.475 mL Type I water and 0.4 mL NH_4OH with the assistance of ultrasonication to produce the Ge^{4+} precursor. 1.6 g $Mg(NO_3)_2{\cdot}6H_2O$ was dissolved separately in 10 mL Type I water and then added to the Ge^{4+} solution. After that, 125 μm $MnCl_2{\cdot}4H_2O$ (0.5 mol L^{-1}) were then added to the above solution, and the pH was adjusted to 8 using NH_4OH. The solution was stirred for two hours and transferred into a Teflon-lined autoclave for hydrothermal treatment at 200 °C for 12 hours. After the reaction was complete, the solid was collected by centrifuging at 8000 rpm for 3 minutes. The products were washed three times with Type-I water and calcinated at 1050 °C for 2 hours. The crude products were then suspended into 5 mM NaOH and ultrasonicated for 1 h to remove the GeO_2 byproduct. After that, the sample was washed three times with Type-I water and dried at 60 °C.

Morphology, structure and optical characterization under normal pressure

The morphologies of the MGO:Mn NPs were characterized using a transmission electron microscope (TEM, Philips CM10 TEM, Philips Electronics, Eindhoven, The Netherlands). The crystal structure was examined using laboratory X-ray diffraction with an Inel XRG3000 generator and an Inel CPS 120 detector (Cu Kα sealed tube source). Photoluminescence spectroscopy was measured using a fibre-optic spectrometer (Avantes, AvaSpec-ULS2048XL-EVO). A 254 nm UV LED light was used as an excitation source.

High pressure *in situ* measurements

Two sets of DAC with different types and culet sizes of diamonds were utilized to achieve static high pressure. The DAC with a pair of type-I diamonds with a culet size of 400 was used for *in situ* high-pressure microdiffraction, Raman and photoluminescence (PL) measurements. For synchrotron far IR measurements, the DAC with a pair of type-II diamonds with a 600 μm culet size was utilized. The stainless-steel gaskets were prepared by pre-indentation to the thickness of 50–70 μm, followed by the drilling of a hole as the chamber. The diameters of the chambers are 150 and 210 μm for the culet sizes of 400 and 600 μm, respectively. A few ruby chips were loaded to calibrate the internal pressure within the sample chamber by ruby fluorescence. Silicon oil was utilized as the pressure transmitting medium (PTM) for *in situ* high-pressure microdiffraction. For *in situ* Raman and PL measurements, the sample was loaded without PTM. Spectral grade polyethylene was used as PTM and spacer for synchrotron far IR measurements.

In situ angle-dispersive microdiffraction was performed at the high energy wiggler (WHE) beamline of the Brockhouse X-ray Diffraction and Scattering (BXDS) sector of the Canadian Light Source (CLS). The wavelength of the monochromatic X-ray beam was 0.3497 Å with a beam size of ~50 μm both horizontally and vertically guided by a pinhole. The diffraction geometry was calibrated using a nickel powder standard. The 2D Debye–Scherrer diffraction patterns were collected using a Varex XRD 4343CT area detector. The 2D diffraction images were integrated into 1D powder patterns using the Dioptas program[55] for further analysis. The 1D XRD patterns were analyzed with the Rietveld refinement method using GSAS-II software.[56]

The *in situ* high-pressure Raman measurements were performed using a customized Raman spectrometer. A diode-pumped solid-state green laser with λ = 532 nm was used as an excitation source. The sample-loaded DAC was aligned using an Olympus microscope toward a focused laser beam (<5 μm) with back-scattering geometry. The spectrometer was calibrated by neon emission lines. The signal was recorded using an ultrasensitive, liquid-nitrogen-cooled, back-illuminated CCD detector, charge-coupled device detector from Acton Spectra Pro 2500i. A grating with 1200 lines per mm was applied to all measurements.

Synchrotron far IR measurements were performed at the far-IR beamline of the Canadian Light Source (CLS). Briefly, an intense far-IR radiation source in the 7–25 cm^{-1} region from coherent synchrotron radiation is directed to a Bruker IFS 125 HR spectrometer. The combination of a 6 μm Mylar beamspliter with a cryogen free superconducting Niobium TES bolometer detector system from QMC Instruments allows the effective collection in the far-IR range of 30–600 cm^{-1}. A horizontal microscopic system equipped with a reflective objective with a large working distance of 47 mm allows the DAC to be aligned with precision. The horizontal microscope is purged with continuous-flow dry nitrogen gas to remove moisture and CO_2.

The *in situ* photoluminescence (PL) measurements were performed using the same spectrometer in the Raman system. A diode-pumped solid-state UV laser with λ = 360 nm was used as an excitation source. A grating with 300 lines per mm was applied to all measurements.

Author contributions

Yihong Liu: methodology, formal analysis, investigation, writing – original draft, Jingyan Liu: investigation, Xiaoran Chen: investigation, Aditya Kutty: investigation, Shanheng Yin: investigation, Lijia Liu: conceptualization, methodology, investigation, formal analysis, writing – review & editing, supervision, funding acquisition. Yang Song: conceptualization, methodology, investigation, formal analysis, writing – review & editing, supervision, funding acquisition.

Conflicts of interest

The authors declare that they have no conflicts.

Data availability

The data that support the findings of this study are available within the article and its ESI† and are available from the corresponding author upon reasonable request.

Acknowledgements

This work is funded by the Natural Sciences and Engineering Research Council Canada through the Discovery Grant (DG) Program (L. L. RGPIN-2020-06675, Y. S. RGPIN-2020-06422) and the Western Strategic Support for NSERC Success Fund. The authors acknowledge support from Soochow University – Western University Centre for Synchrotron Research (SWC) at Western University. Canadian Light Source, a national research facility of the University of Saskatchewan, is supported by the Canada Foundation for Innovation (CFI), the Natural Sciences and Engineering Research Council (NSERC), the National Research Council (NRC), the Canadian Institutes of Health Research (CIHR), the Government of Saskatchewan, and the University of Saskatchewan. Y. Liu acknowledges the receipt of support from the CLSI Student Travel Support Program. Thanks to Dr AI Rahemtulla and Graham King at the Brockhouse

Diffraction Sector beamline, as well as Dr Jianbao Zhao at the far-IR beamline for their technical support.

References

1 L. Zhang, Y. Wang, J. Lv and Y. Ma, *Nat. Rev. Mater.*, 2017, **2**, 1–16.
2 L. Meng, T. V. Vu, L. J. Criscenti, T. A. Ho, Y. Qin and H. Fan, *Chem. Rev.*, 2023, **123**, 10206–10257.
3 L. Wang, Z. Wu, G. Gao and Y. Tian, *Adv. Funct. Mater.*, 2024, **34**, 2411463.
4 T. Yagi, T. Sakai, H. Kadobayashi and T. Irifune, *High Press. Res.*, 2020, **40**, 148–161.
5 L. Marciniak, P. Woźny, M. Szymczak and M. Runowski, *Coord. Chem. Rev.*, 2024, **507**, 215770.
6 H. Mao, J.-A. Xu and P. Bell, *J. Geophy. Res. Solid Earth*, 1986, **91**, 4673–4676.
7 T. H. Maiman, R. Hoskins, I. d'Haenens, C. K. Asawa and V. Evtuhov, *Phys. Rev.*, 1961, **123**, 1151.
8 M. Runowski, P. Wozny, N. Stopikowska, Q. Guo and S. Lis, *ACS Appl. Mater. Interfaces*, 2019, **11**, 4131–4138.
9 G. Shen, Y. Wang, A. Dewaele, C. Wu, D. E. Fratanduono, J. Eggert, S. Klotz, K. F. Dziubek, P. Loubeyre and O. V. Fat'yanov, *High Press. Res.*, 2020, **40**, 299–314.
10 M. Szymczak, M. Runowski, V. Lavín and L. Marciniak, *Laser Photonics Rev.*, 2023, **17**, 2200801.
11 J. Barnett, S. Block and G. Piermarini, *Rev. Sci. Instrum.*, 1973, **44**, 1–9.
12 B. Lorenz, Y. Shen and W. Holzapfel, *High Press. Res.*, 1994, **12**, 91–99.
13 M. Runowski, A. Shyichuk, A. Tyminski, T. Grzyb, V. Lavín and S. Lis, *ACS Appl. Mater. Interfaces*, 2018, **10**, 17269–17279.
14 S. Adachi, *J. Lumin.*, 2023, **263**, 119993.
15 L.-I. Bulyk, L. Vasylechko, V. Mykhaylyk, C. Tang, Y. Zhydachevskyy, Y. Hizhnyi, S. Nedilko, N. Klyui and A. Suchocki, *Dalton Trans.*, 2020, **49**, 14268–14279.
16 T. Zheng, M. Runowski, I. R. Martín, K. Soler-Carracedo, L. Peng, M. Skwierczyńska, M. Sójka, J. Barzowska, S. Mahlik and H. Hemmerich, *Adv. Mater.*, 2023, **35**, 2304140.
17 Q. Zeng, M. Runowski, J. Xue, L. Luo, L. Marciniak, V. Lavín and P. Du, *Adv. Sci.*, 2024, **11**, 2308221.
18 M. Ayvacıkli, Z. Kotan, E. Ekdal, Y. Karabulut, A. Canimoglu, J. G. Guinea, A. Khatab, M. Henini and N. Can, *J. Lumin.*, 2013, **144**, 128–132.
19 W. Xiao, F. Lei, L. Yin, Y. Shi, J. Xie and L. Zhang, *Solid State Sci.*, 2017, **72**, 116–123.
20 E. Song, X. Jiang, Y. Zhou, Z. Lin, S. Ye, Z. Xia and Q. Zhang, *Adv. Opt. Mater.*, 2019, **7**, 1901105.
21 M. Runowski, J. Marciniak, T. Grzyb, D. Przybylska, A. Shyichuk, B. Barszcz, A. Katrusiak and S. Lis, *Nanoscale*, 2017, **9**, 16030–16037.
22 C. V. Stan, R. Dutta, R. J. Cava, V. B. Prakapenka and T. S. Duffy, *Inorg. Chem.*, 2017, **56**, 8026–8035.
23 N. L. Ross and A. Navrotsky, *Am. Mineral.*, 1988, **73**, 1355–1365.
24 G. Viola, F. D'Isanto, V. Koval, G. Cempura, H. Yan, F. Smeacetto and M. Salvo, *Ceram. Int.*, 2019, **45**, 7878–7884.
25 M. Iwasaki, D. N. Kim, K. Tanaka, T. Murata and K. Morinaga, *Sci. Technol. Adv. Mater.*, 2003, **4**, 137–142.
26 S. Zheng, J. Shi, X. Fu, C. Wang, X. Sun, C. Chen, Y. Zhuang, X. Zou, Y. Li and H. Zhang, *Nanoscale*, 2020, **12**, 14037–14046.
27 J. Yang, Y. Zhou, H. Ming, E. Song and Q. Zhang, *ACS Appl. Electron. Mater.*, 2022, **4**, 831–841.
28 Y. Liu, J. A. McLeod, L.-Y. Chang, C.-K. Chang, Y. Jiang, Z. Wang, A. Lefebvre, X. Chen and L. Liu, *Mater. Today Commun.*, 2024, **38**, 108080.
29 Y. Liu, J. Sun, Y. Jiang, G. Fanchini, W. Zhu, L. V. Goncharova and L. Liu, *ACS Appl. Nano Mater.*, 2024, **7**, 11541–11552.
30 T. Yamanaka, M. Hirano and Y. Takeuchi, *Am. Mineral.*, 1985, **70**, 365–374.
31 P. Gillet, A. Le Cléac'h and M. Madon, *J. Geophy. Res. Solid Earth*, 1990, **95**, 21635–21655.
32 G. H. Wolf, S. Wang, C. A. Herbst, D. J. Durben, W. F. Oliver, Z. Kang and K. Halvorson, *High Press. Res. Appl. To Earth Planet. Sci.*, 1992, **67**, 503–517.
33 Y. Liu, L.-Y. Chang, L.-C. Hsu, M. C. Adam, Y. Jiang, L. V. Goncharova and L. Liu, *J. Alloys Compd.*, 2023, **957**, 170422.
34 A. C. Strzelecki, X. Zhao, J. L. Baker, P. Estevenon, T. Barral, A. Mesbah, D. Popov, S. Chariton, V. Prakapenka and S. Ahmed, *J. Phys. Chem. C*, 2023, **127**, 4225–4238.
35 H. Chen, L. Wang, J. Bai, J. C. Hanson, J. B. Warren, J. T. Muckerman, E. Fujita and J. A. Rodriguez, *J. Phys. Chem. C*, 2010, **114**, 1809–1814.
36 S. Klotz, J. Chervin, P. Munsch and G. Le Marchand, *J. Phys. D: Appl. Phys.*, 2009, **42**, 075413.
37 Z. Dong and Y. Song, *Chem. Phys. Lett.*, 2009, **480**, 90–95.
38 Z. Dong and Y. Song, *Appl. Phys. Lett.*, 2010, **96**, 151903.
39 Z. Dong, K. K. Zhuravlev, S. A. Morin, L. Li, S. Jin and Y. Song, *J. Phys. Chem. C*, 2012, **116**, 2102–2107.
40 Z. Dong and Y. Song, *Can. J. Chem.*, 2015, **93**, 165–172.
41 Z. Dong, F. Xiao, A. Zhao, L. Liu, T.-K. Sham and Y. Song, *RSC Adv.*, 2016, **6**, 76142–76150.
42 Y. Usui, J. Tsuchiya and T. Tsuchiya, *Geophy. Res. Solid Earth*, 2010, **115**, B03201.
43 Y. Wang, T. Seto, K. Ishigaki, Y. Uwatoko, G. Xiao, B. Zou, G. Li, Z. Tang, Z. Li and Y. Wang, *Adv. Funct. Mater.*, 2020, **30**, 2001384.
44 Z. Zheng, Y. Song, B. Zheng, Y. Zhao, Q. Wang, X. Zhang, B. Zou and H. Zou, *Inorg. Chem. Front.*, 2023, **10**, 2788–2798.
45 Z. Zheng, Z. Li, H. Zou, Q. Tao, Y. Zhao, Q. Wang, Z. Shi, Y. Song and L. Li, *Inorg. Chem.*, 2024, **63**, 3882–3892.
46 Y. Cao, G. Qi, L. Sui, Y. Shi, T. Geng, D. Zhao, K. Wang, K. Yuan, G. Wu and G. Xiao, *ACS Mater. Lett.*, 2020, **2**, 381–388.
47 M. Runowski, P. Woźny, K. Soler-Carracedo, A. Lazarowska, M. Kamiński, N. Majewska, A. Muñoz, J. Moszczyński, S. Sobczak and K. Dave, *Mater. Horiz.*, 2024, **11**, 4911–4924.
48 T. Zheng, J. Luo, D. Peng, L. Peng, P. Woźny, J. Barzowska, M. Kamiński, S. Mahlik, J. Moszczyński and K. Soler-Carracedo, *Adv. Sci.*, 2024, **11**, 2408686.

49 D. Zhang, B. Zheng, Z. Zheng, L. Li, Q. Yang, Y. Song, B. Zou and H. Zou, *Chem. Eng. J.*, 2022, **431**, 133805.
50 T. Zheng, L. Luo, P. Du, S. Lis, U. R. Rodríguez-Mendoza, V. Lavín and M. Runowski, *Chem. Eng. J.*, 2022, **446**, 136839.
51 Q. Wang, H. Zou, T. Gao, S. Chen, G. Zhu and C. Liu, *Ceram. Int.*, 2023, **49**, 31701–31710.
52 K. Su, L. Mei, Q. Guo, P. Shuai, Y. Wang, Y. Liu, Y. Jin, Z. Peng, B. Zou and L. Liao, *Adv. Funct. Mater.*, 2023, **33**, 2305359.
53 J. Huang, P. Jiang, Z. Cheng, R. Wang, R. Cong and T. Yang, *Inorg. Chem. Front.*, 2023, **10**, 2776–2787.
54 Z. Chen, S. Du, F. Li, S. Zhang, S. Zhao, Z. Tian, J. Zhang, X. Yuan, G. Liu and K. Chen, *J. Mater. Sci. Technol.*, 2024, **194**, 98–109.
55 C. Prescher and V. B. Prakapenka, *High Press. Res.*, 2015, **35**, 223–230.
56 B. H. Toby and R. B. Von Dreele, *J. Appl. Crystallogr.*, 2013, **46**, 544–549.